Epitaxial growth of the intermetallic compound NiAl on low-index Ni surfaces in Ni/Al reactive multilayer nanofoils

Florence Baras, O. Politano

Epitaxial growth of the intermetallic compound NiAl on low-index Ni surfaces in Ni/Al reactive multilayer nanofoils

F. Baras and O. Politano

January 19, 2022

Crystal growth in the case of self-propagating reactions in Ni-Al nanofoils was investigated by means of molecular dynamics simulations. We studied the heteroepitaxial growth of NiAl on Ni during mixing and alloying at interfaces. Three low-index Ni surfaces were considered. In the case of the (001) and (111) orientations of Ni, a layer-by-layer formation occurred. Four orientations of NiAl grains were observed in (001) and six in (101). The orientation relationships of NiAl(101) with Ni(001) and with Ni(111) were derived. For the (101) orientation of Ni, massive crystallization was observed in the form of grains tilted in relation to the interface. The microstructure evolution was tracked along with grain orientation dynamics. In all cases, a simple geometric construction based on the relationship between unit cells of Ni and NiAl explains crystal growth specificities. The nucleation process and growth kinetics were also investigated. The present study proves that crystal growth varies considerably, in relation to Ni orientation.

1 Introduction

Since the first elaboration of Ni/Al nanofoils [1], reactive multilayer nanofoils (RMNF) have continued to arouse interest because of their very specific characteristics. These RMNFs are composed of hundreds of stacked thin metallic layers, varying in thickness from 4 to 100 nm.

After being initiated at one edge of the sample, an alloying reaction propagates in a self-sustaining way, without any further supply of heat because of the exothermic character of the process. The reaction starts at a relatively low temperature (600 K) and proceeds quite rapidly (up to 10 m/s or even more) in comparison with the same process in micrometric metallic powder mixtures. As a consequence, RMNFs are used for joining applications [2] or as energetic materials [3].

Extremely rapid gasless reactions in Ni-Al reactive multilayer nanofoils have been investigated both experimentally and theoretically [4, 5]. By quenching the fast reaction wave, the microstructure along the arrested front can be studied at micro- and

nanoscales. The typical microstructure consists of NiAl intermetallic grains hanging on to the interfaces, as shown in Fig. 1. The underlying mechanism was found to be a suc-

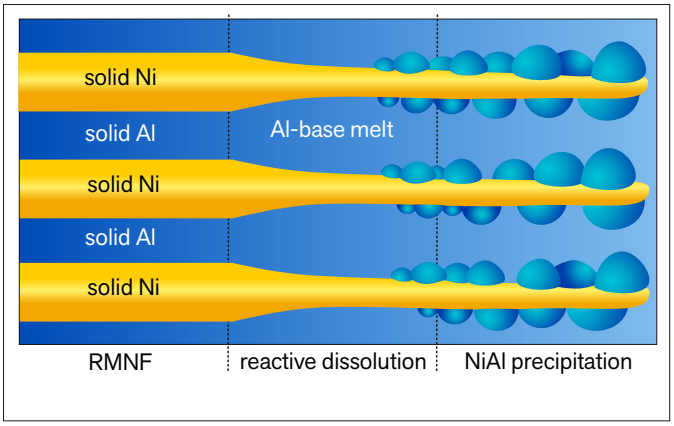

Figure 1: Schematic illustration of a self-sustaining front in RMNF. Blue and yellow layers correspond to Al and Ni, respectively. The preheating zone is made of alternating reactants, while the afterburning zone is filled with grains of NiAl. For interpretation of the reference to color in this figure legend, the reader is referred to the web version of this article.

cession of transformations: melting of the aluminum layer, partial dissolution of nickel into liquid aluminum, and formation of intermetallics:

$$\mathrm{Ni}(s) + \mathrm{Al}(s) \rightarrow \mathrm{Ni}(s) + \mathrm{Al}(m) \rightarrow \mathrm{Ni}(s) + \mathrm{AlNi_x}(m) \rightarrow \mathrm{Ni}(s) + \mathrm{NiAl}(s) \qquad (1)$$

where s is solid and m is melted. The solid grains of the NiAl phase, if present, do not form a continuous interface layer at the Ni/Al boundary, but exhibit different crystallographic orientations, and remain separated by liquid/amorphous interlayers. These experimental features raise questions about the nucleation and growth of the NiAl phase in a $\mathrm{AlNi_x}(m)$ solution surrounded by solid Ni layers. Phase transformation proceeds through heterogeneous nucleation: no grains formed spontaneously in the bulk of the liquid layer.

To some extent, the alloying reaction at interfaces in RMNF can be compared to the growth of new compounds during thin-film deposition. For heteroepitaxial growth, e.g. A on substrate B, the behavior of A adatoms is strongly dependent on energy considerations and lattice mismatch or surface diffusion. For metals with alloying, the heteroepitaxial growth of A on B with intermixing processes produces (A+B)/B binary alloy surface structures. Experiments (e.g. XPS, STM, Auger electron spectroscopy, etc.) have investigated the dynamics of structure formation in the very first film layers [6]. The growth mode of islands (2D, 3D or 2D-3D transitions) controls nanostructures on surfaces [7].

Thin-film deposition in the Ni+Al system is well documented in the case of Ni on Al, and for Al on Ni. Deposition of Ni on Al(100) was considered in [8]. Molecular dynamics simulations have shown that the orientation of the Al interface plays a role in film surface

roughness [9]. In the case of complex codeposition of Ni and Al on the intermetallic NiAl(110) substrate, the formation of non-equilibrium nanostructures is promoted [6]. Growth of Ni_3Al and NiAl alloys on Ni(111) from ultra-thin Al deposits was studied in [10, 11]. In all these studies, the formation of surface compounds was found to depend on deposition conditions (e.g. coverage, annealing temperature, film thickness, etc.), epitaxial relationships, and local composition. Although there is a striking analogy between our problem and thin-film deposition, the conditions and processes involved are drastically different, as we will show. Martensite nucleation from austenite also involves the formation of the bcc-phase from the fcc-phase. In this case, a Molecular Dynamics study provided the mechanism for the fcc $\rightarrow$ bcc transformation [12].

This work presents an accurate study of the dynamics of structural transformation in nanolayers. We investigated the role played by the interface and by the underlying solid substrate. Both the geometric and energetic aspects of NiAl nucleation in Ni-Al nanofoils were elucidated. Understanding the epitaxial growth of NiAl grains on a solid Ni substrate in SHS propagation is the main focus of this study.

In section 2, we give details of the simulations. The results are presented in section 3. The specific problem of epitaxial NiAl growth on solid Ni is examined. Three low-index orientations of the Ni substrate were considered: Ni(001), Ni(111), and Ni(101). The case of Ni(101) is more complicated, requiring a texture analysis that is discussed in the last part of the section. Observations are presented together with suitable analyses. Finally, the very first stages of nucleation are revisited.

2 Simulation details

Molecular dynamics simulations (MD) were set up to represent experimental conditions as closely as possible. The layered Ni-Al system consists of at least one layer of fcc-Al (face-centered cubic Al) between two layers of fcc-Ni (Fig. 2a) Time evolution of this simplified geometry was then tracked using the LAMMPS software package [13], with an embedded-atom method (EAM) potential for Ni-Al [14]. This potential, developed by Mishin et al., was constructed by fitting to experimental properties and ab initio data for the B2-NiAl compound, pure Ni, and pure Al [15]. The potential provides an effective description of the B2-NiAl and L12-Ni3Al structures, and is commonly used to study the reactivity ofNi/Al nano-multilayers [16]. However, we note that this EAM potential does not reproduce the Al-rich equilibrium phases found within the Ni/Al binary system, and may thus induce a bias in MD observations by facilitating the formation of the most stable intermetallic compound, NiAl. The formation of transient Al-rich compounds might not be captured by these simulations.

For the simulations, the equations of motion are integrated with a time step of 0.002 ps. The Nosé-Hoover and Parrinello-Rahman formalisms were used for equilibration runs, and for production runs in the NPT (isothermal-isobaric) or NVT (canonical) ensembles. The resulting microstructures were analyzed with the Ackland and Jones approach, which allows the local environment for each atom to be obtained [17]. This method is based on the angle distribution of the nearest neighbors of each atom, and

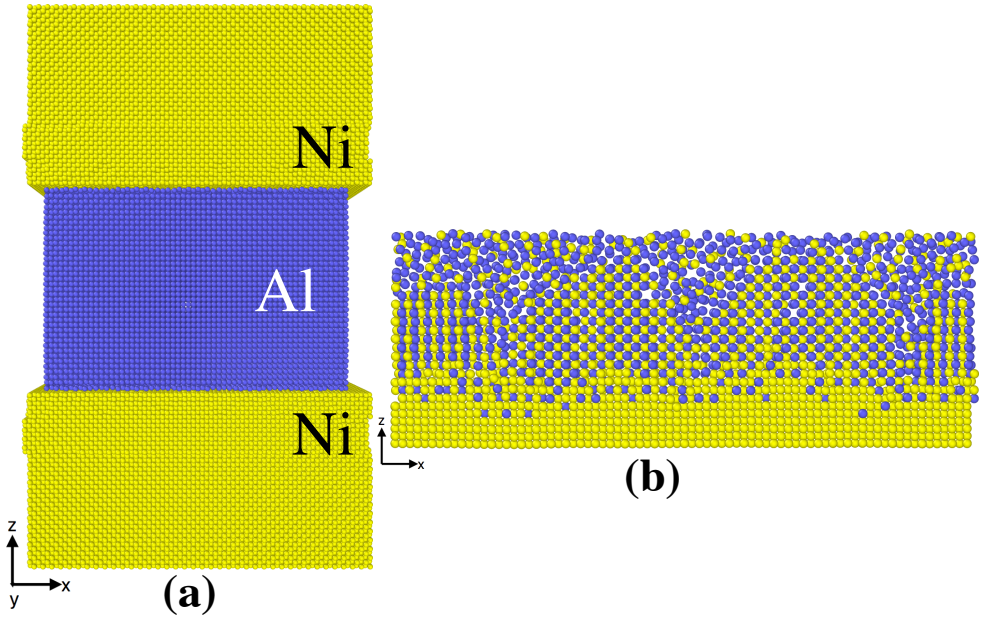

Figure 2: (a) Initial configuration of the simulated system, with one Al slice in between two Ni layers. Al and Ni are shown as blue and yellow spheres respectively. The typical size of the simulation box is $L_x = L_y = 13.6$ nm and $L_z = 22.3$ nm. The system is composed of 316 602 atoms. (b) Snapshot of the system at $t = 20$ ns, near the lower interface. For better visualization, only a 10 $\mathring{A}$ slice along the y axis is shown. (For interpretation of the references to color in the figure legend, the reader is referred to the web version of this article.)

indentifies fcc metals as well as intermetallic phases (i.e. B2-NiAl with bcc (body-centered cubic) stacking, and L12-Ni_3Al with fcc stacking). We conducted isothermal-isobaric (NPT) simulations with barostating and thermosetting time scales, equal to 2.0 ps and 0.2 ps, respectively. As mentioned above, the reaction front in the nanofoil propagates extremely fast ($\sim$ 1 -10 m/s), and is characterized by high temperatures. The reaction front traverses a sample 10 nm long in less than 1 ns, quickly raising its temperature to a high value. A set of simulations at constant high temperature was therefore carried out in order reproduce the sample just behind the propagation, revealing the mechanisms associated with the nucleation and growth of the product phases.

3 Results

As shown in [4, 5], the specific scheme observed during the solid/liquid reaction in the reaction wave reads:

1. melting of the Al layer;

2. dissolution of Ni into the Al liquid layer, mixing of Ni and Al atoms,

3. creation of vacancies in the Ni solid substrate,

4. diffusion of Al in the solid substrate and diffusion of Ni in the liquid layer,

5. reaction at the interface between Ni and Al, and formation of the intermetallic compound NiAl

At stage 5, the NiAl-B2 phase nucleates and grows. The round grains observed are disoriented relative to each other, and separated by liquid/amorphous interlayers. The morphology of the product is characteristic of a *mosaic dissolution-precipitation* mechanism [5]. Because of their different orientations, the grains do not coalesce to form a continuous layer of NiAl at the interface. Once a seed forms at the interface, the grain grows due to precipitation of the Ni atoms present in the liquid Ni+Al. During the growth process, the channels between the grains allow Ni to dissolve into the melt by means of liquid-state mass transfer, which is much faster than solid-state diffusion across the intermetallic compound. Progressive dissolution sustains growth.

These results indicate that the interface between solid Ni and liquid Al plays a crucial role in the nucleation of the first seeds at very short times. We will demonstrate the role of the Ni interface orientation in the selection of a specific grain orientation. Then we will consider the problem of growth according to the orientation of the Ni surface. Both analyses explain the complex mechanisms that lead to the characteristic morphology observed experimentally.

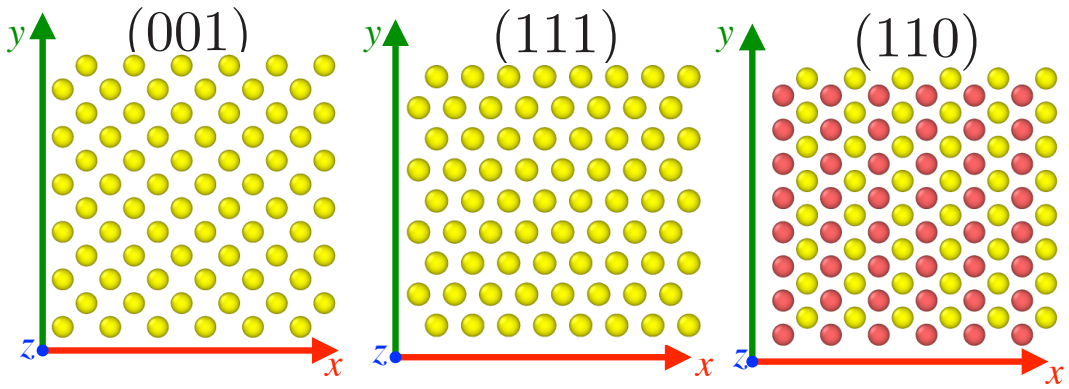

Figure 3: The three surface orientations of solid Ni (top view). The Ni atoms at the interface are shown as yellow spheres. The red spheres correspond to Ni atoms belonging to the plane just below the interface. (For interpretation of the references to color in the figure legend, the reader is referred to the web version of this article.)

3.1 Ni-substrate in orientation (001)

We first consider the case where the interface is oriented normal to the [001] direction. During grain growth, the intermetallic phase NiAl appears plane by plane. In the following, we will adopt the usual terminology. The new phase that appears, NiAl, is referred

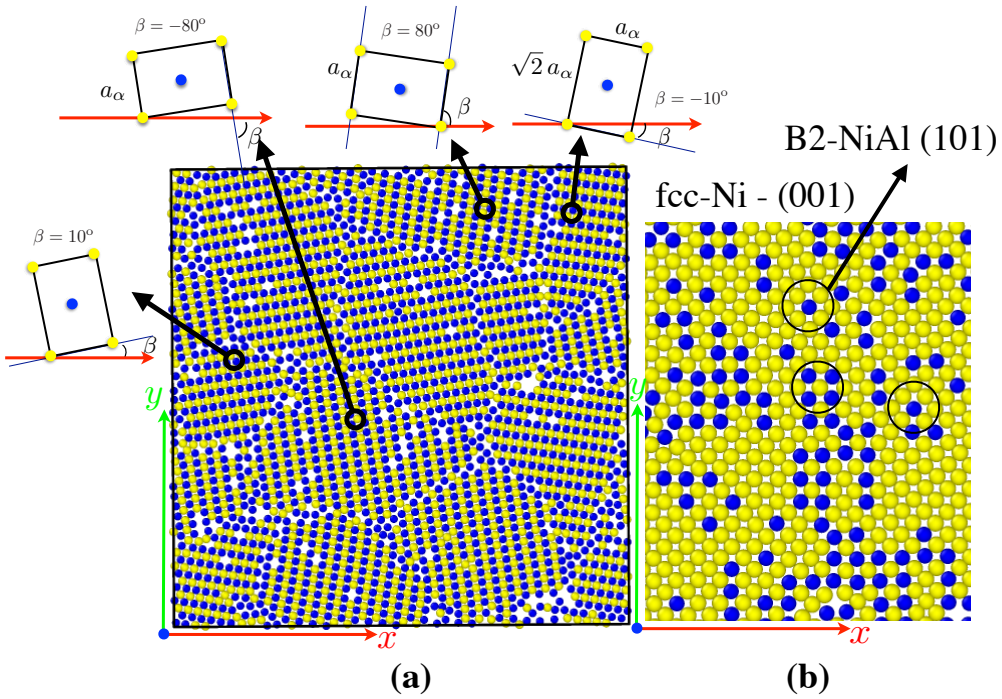

Figure 4: (a) Snapshot of a (001)-slice across the new NiAl phase, parallel to the interface, at $t = 25$ ns. The Al and Ni atoms are shown as blue and yellow spheres, respectively. The four orientations observed in the simulations are represented. (b) Section of an atomic plane at the beginning of the nucleation process. (For interpretation of the reference to color in this figure legend, the reader is referred to the web version of this article.)

to as the α-phase, and the substrate Ni as the γ-phase. Fig. 4a shows the arrangement of atoms in one atomic plane parallel to the interface. The atomic arrangement is characteristic of the (110) orientation in NiAl. Note that this orientation corresponds to the lowest surface energy for the NiAl system [18]. This plane (110) of the NiAl phase (α-phase) is parallel to the plane (001) of the fcc-Ni parent phase (γ-phase). In each plane, small grains of NiAl form, and are separated by grain boundaries. The grain orientation is not random. Depending on the atomic positions in the plane, only four rectangular unit cells were detected, as depicted in Fig. 4a. Each unit cell can be identified by the orientation of the rectangular unit cell. This orientation, marked by the angle β, is simply the direction drawn between the closest atoms of same species (Ni, for instance). The angle β is defined as the angle between this direction and the x-axis.

We will show that the growth of NiAl is epitaxial. The lattice parameters of Ni (γ-phase) and NiAl (α-phase) at 1000 K [14] are:

$$a_\gamma = 3.5075 \ \mathring{A} \tag{2}$$

$$a_\alpha = 2.9072 \ \mathring{A} \tag{3}$$

and satisfy the relation:

$$\sqrt{2}a_\gamma \approx \sqrt{3}a_\alpha \tag{4}$$

The relation (4) implies that the diagonal ℓ_γ of a square unit cell in the plane $(001)_\gamma$ is equal to the diagonal ℓ_α of a rectangular unit cell in the plane $(110)_\alpha$. Fig. 4b shows the snapshot of an atomic place of (001)-Ni at the beginning of the nucleation process. Due to dissolution, some interfacial Ni atoms ~~quit~~ move from this atomic plane to reach the liquid phase, and so the vacancies created can be occupied by incoming Al atoms, as shown in Fig. 4b. This substitution is possible because the distance between the nearest neighbors Ni atoms on the diagonal (γ-phase) is the same as for the Ni and Al atoms (α-phase) (eq. (4)). Assuming that a central atom of Ni of the unit γ-cell is replaced by an atom of Al, it is easy to describe how epitaxial growth can occur.

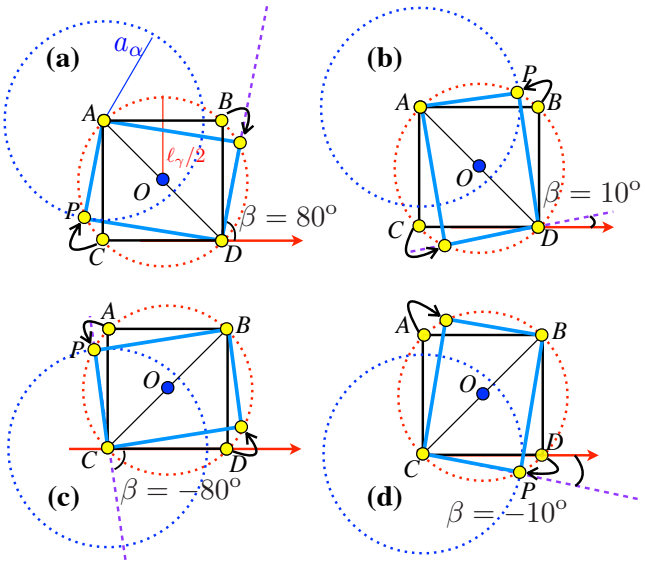

Figure 5: The four orientations of the 2D α-cell with respect to the 2D γ-cell. The square γ-cell is represented in black, while the rectangular α-cell is in blue (gray) . The central atom (located in 0) is a Ni atom in the γ-cell and an Al atom in the α-cell. For interpretation of the reference to color in this figure legend, the reader is referred to the web version of this article.

The square γ-cell is inscribed in a circle of diameter ℓ_γ. For any point P on this circle, $\widehat{APD}$ is a rectangle triangle where A and D are the vertices of the square located on the selected diagonal (Fig. 5a). A circle of radius a_α is plotted around a vertex, for example A. The point P is the intersection between the two circles. The triangle $\widehat{APD}$ and its symmetrical with respect to the diagonal form a rectangular 2D α-cell in a (110) plane. Four possible options exist: either choose the other intersection between the two circles (Fig. 5b), or perform the same constructions using the other diagonal (Fig. 5c and 5d). Fig. 6a shows the histogram of the orientation of closest neighbors of the same species, β, in the crystallized phase NiAl at the (001)-Ni interface, as measured in MD simulations. As expected, four peaks are observed within the context of the previous

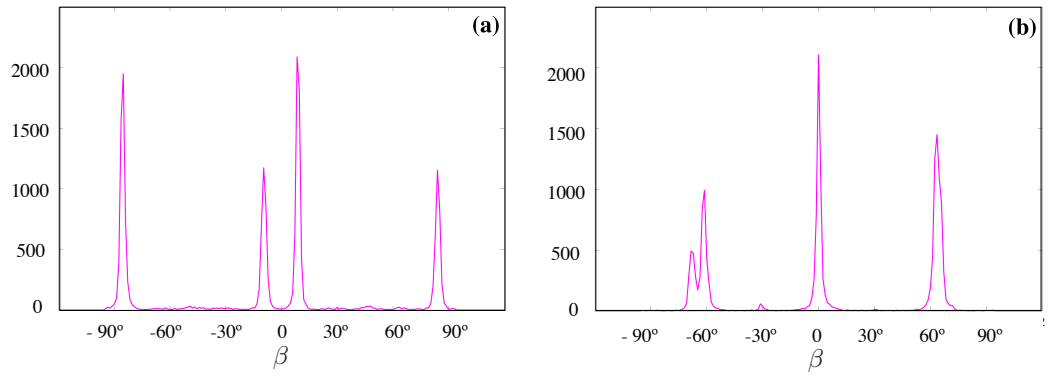

Figure 6: Histogram of the orientation of NiAl-grains in the case of the (001) Ni-interface (a) and the (111) Ni-interface (b).

analysis.

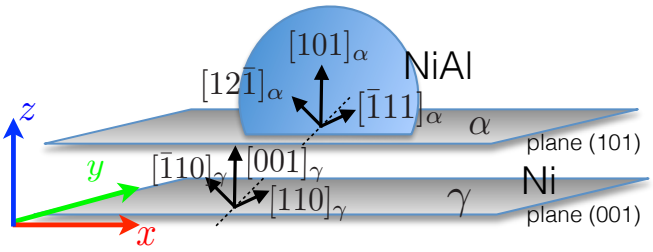

Figure 7: Schematic illustration of the epitaxial growth of NiAl at the interface.

The NiAl(101)(α)− and Ni(001)(γ)−lattices are thus related by an orientation relationship:

$$[001]_\gamma \parallel [101]_\alpha \tag{5a}$$
$$[\bar{1}10]_\gamma \parallel [12\bar{1}]_\alpha \tag{5b}$$
$$[110]_\gamma \parallel [\bar{1}11]_\alpha \tag{5c}$$

In the plane $(101)_\alpha$, the direction $[\bar{1}11]_\alpha$ corresponds to the diagonal of the 2D α-cell. The vectors are orthogonal 2 by 2. The choice (5c) is not unique: the "other" diagonal of the 2D γ-cell could be chosen:

$$[\bar{1}10]_\gamma \parallel [\bar{1}11]_\alpha \tag{5d}$$

Figure 7 shows a single grain of NiAl oriented with respect to the underlying Ni substrate.

The transformation from fcc lattice (γ-phase) to bcc lattice (α-phase) is well documented in physical metallurgy, in the specific case of transformation from austenite to martensite [20]. Relation 5 corresponds to a Pitsch transformation [21]. In the case of NiAl epitaxial growth, a similar transformation involves atoms located at the interface,

and induces a slight deformation of the planar unit cell, in order to adjust the NiAl lattice to the underlying Ni lattice. Following [20], the explicit form of the coordinate transformation was derived in the case of the Ni/NiAl transformation. The coordinate transformation $(\alpha J\gamma)$ can be used to find the components of any vector u in the α-basis, given its components in the γ-basis:

$$[\alpha; u] = (\alpha J\gamma)[\gamma; u] \tag{6a}$$

where $[A; u] = [u_1, u_2, u_3]$ represents a column vector with respect to the A-basis. Reciprocally

$$[\gamma; u] = (\gamma J\alpha)\,[\alpha; u] \tag{6b}$$

with $(\gamma J\alpha) = (\alpha J\gamma)^{-1}$. Finding the coordinate transformation $(\alpha J\gamma)$ proves the existence of an epitaxial relation between the Ni and NiAl crystallographic structures. The derivation is presented in appendix A. The matrix $(\alpha J\gamma)$ reduces to a matrix product of two rotations:

$$(\alpha J\gamma) = R_y(\theta) \cdot R_z(\varphi) \tag{7}$$

where the rotation R_z around the z-axis with an angle φ is followed by a rotation R_y around the y-axis with an angle θ (see Table 1).

Diagonal of γ cell	θ	φ
$[110]_\gamma$	$\pi/4$	$1.7407\,(100°)$
$[110]_\gamma$	$-3\pi/4$	$-0.1699\,(-9.74°)$
$[\bar{1}10]_\gamma$	$\pi/4$	$0.1699\,(9.74°)$
$[\bar{1}10]_\gamma$	$-3\pi/4$	$1.4001\,(80°)$

Table 1: Euler angles θ and φ of the coordinate transformation $(\alpha J\gamma) = R_y(\theta) \cdot R_z(\varphi)$ for the two choices of diagonal for the γ square unit cell. The orientation $[\bar{1}11]_\alpha$ of the diagonal of the NiAl cell is fixed.

The epitaxy relation between NiAl-(110) and Ni-(001) is easy to visualize when applying two successive rotations. If we suppose that the γ-phase is fixed, as in the case of the nucleation of NiAl on Ni solid interfaces, eq. (6b) reads $(\gamma J\alpha) = R^{-1} = R_z(-\varphi)\cdot R_y(-\theta)$. Fig. 8 shows the position of the 5 atoms initially located in a the (101) plane after a rotation of $\theta = 3\pi/4$ around the y-axis. A second rotation around the z-axis of angle φ aligns the diagonal of the 2D $\alpha-$unit cell with the diagonal of the square corresponding to the 2D $\gamma-$unit cell. The difference in orientation of the two 2D unit-cells (a square and a rectangle of side a_α and $\sqrt{2}a_\alpha$) with a diagonal of the same length $\sqrt{3}a_\alpha$ is:

$$\delta = \frac{\pi}{4} - \arcsin\left(\frac{1}{\sqrt{3}}\right) = 0.1699 \equiv -\varphi$$

that is precisely the value of the angle φ reported in Table 1. The four orientations observed during the growth process (Fig. 5) are derived in Appendix A and reported in

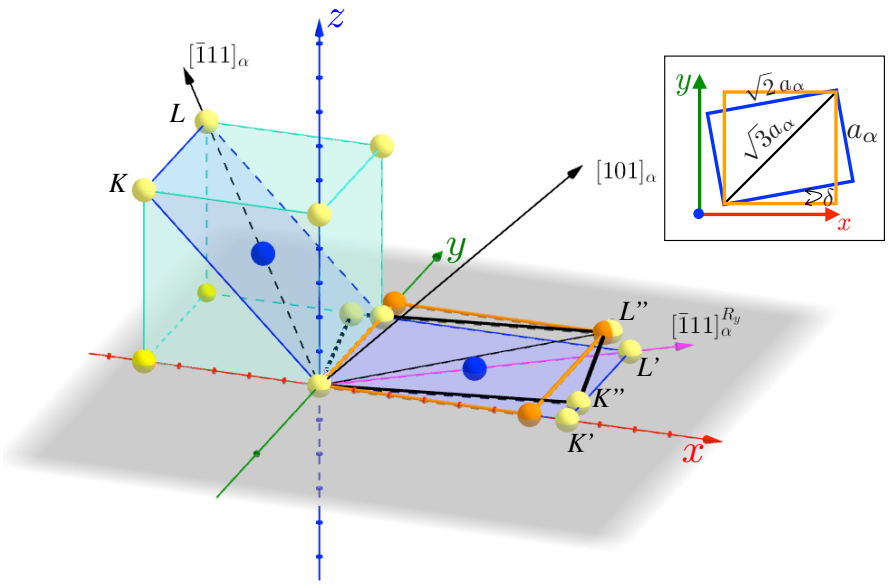

Figure 8: The cube corresponds to a NiAl unit cell. A 2D unit cell of NiAl in the (101) plane is shown in light blue. The positions of the 5 atoms of this cell are plotted before and after the rotation around the y-axis: $K' = R_y(-\theta)K$ and $L' = R_y(-\theta)L$, with $\theta = -3\pi/4$. The direction $[\bar{1}11]_\alpha^{R_y}$ (in magenta) is the new orientation after the rotation $R_y(-\theta)$. The 2D unit cell is then rotated around the z axis: $K'' = R_z(-\varphi)K'$ and $L'' = R_z(-\varphi)L'$, with $\varphi = -0.1699$. Dashed lines indicate "non-visible" lines from this view angle. The gray plane is the "horizontal" xy-plane. The orange square represents the Ni (001) unit lattice. The inset represents the α- and γ-cells in the plane Ni-(001), as plotted in Fig. 5. For interpretation of the reference to color in this figure legend, the reader is referred to the web version of this article.

Table 1. In addition, a new tag corresponding to the local orientation of the grain can be associated with each individual atom. This feature may be helpful for visualization purposes.

Transmission Electron Microscopy (TEM), with associated Electron Diffraction, is a well-established experimental technique that gives an atomistic-scale description of materials. High-resolution TEM was used to determine the local composition and structure of the reaction products along the arrested front in Ni/Al RMNFs (see for instance [4]). In order to provide a useful tool for further experimental investigations, we also developed a diffraction analysis of the system under study. The calculated diffraction pattern of fcc-Ni with zone axis along the [001] direction, shown in Fig. 9a, corresponds to the low surface orientation of solid Ni-[001] in Fig. 3a [22, 23]. The square mesh unit d of the reciprocal lattice is $d = 1/a_\gamma$. The NiAl phase was observed to grow in the [101] direction. The calculated diffraction pattern of bcc-NiAl is depicted in Fig. 9c. Each point of the reciprocal lattice corresponds to an observable peak (hkl). The unit cell of the reciprocal lattice is a rectangle $d \times \sqrt{2}d$ where $d = 1/a_\alpha$. Some representative points are indexed in Fig. 9c. The gray circle around a blue bullet point represents the relative

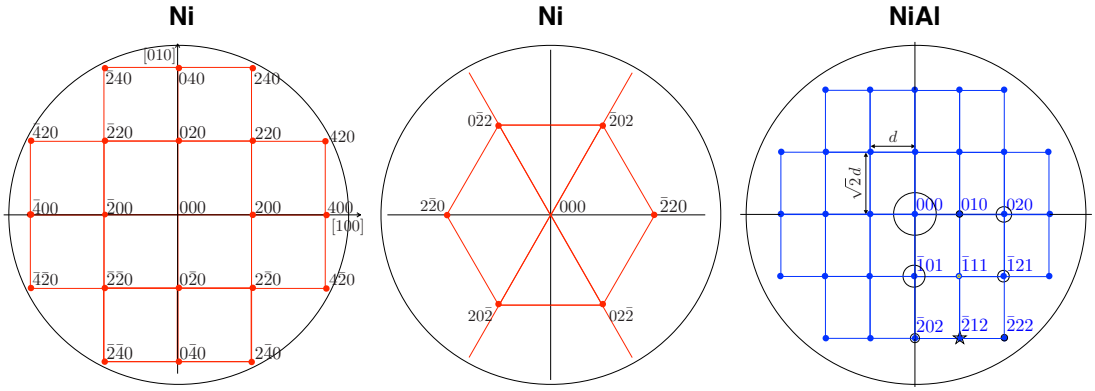

Figure 9: (a-b) Calculated diffraction pattern of fcc-Ni substrate with zone axis aligned along the [001]- and [111]-directions. (c) Calculated diffraction pattern of bcc-NiAl with zone axis aligned along the [101]-direction.

intensity of the diffraction peak. The star indicates a peak of such low intensity that it is invisible. Not all points contribute in an equal manner to the diffraction pattern.

Next, the computational method developed in [24] was applied to produce a virtual electron diffraction pattern directly from atomistic simulations. The virtual diffraction algorithm allows us to connect the atomic configuration obtained by molecular dynamics simulations to experimental studies for the characterization of complex nanoscale materials. The selected-area electron diffraction (SAED) pattern computed for a region of the system, in the z direction, is depicted in Fig. 10a. This section contains a few Ni atomic planes and NiAl grains in the crystallized region. The region is exactly that shown in Fig. 2b. In order to interpret this complex SAED, we calculated the corresponding diffraction pattern. ~~Fig. 10 shows the overlay of the Ni-[001] pattern and four NiAl-[101] rotated patterns. The rotation angles are ±10° and ±80°, as described in our previous analysis.~~ The [001]-Ni pattern was overlaid by four rotated [101]-NiAl patterns (see Fig. 10b). The rotation angles are precisely the ones described in our previous analysis: ±10° and ±80°, as shown in Figs. 4 and 5. For instance, four (020)-NiAl peaks surround the (200)-Ni peak. The virtual SAED pattern is reproduced with striking similarity. The green square defined by the Ni peaks is drawn as a guide to identify the structure. The location of the peaks is similar, as is their intensity, as shown in Fig. 10a by the magenta circles on representative indexed peaks.

3.2 Ni-substrate in orientation (111)

The fcc-Ni parent phase (γ-phase) is close-packed in the (111)-plane, as shown in Fig. 3. The distance between the Ni atoms is $a_\gamma/\sqrt{2} = 2.4621 \approx 2 \times r_{\text{atom}}$, where $r_{\text{atom}} = 1.24 \pm 0.4$ is an estimation of the atomic radius. As in the previous case, the bcc-NiAl phase (α-phase) is formed in (110)-planes, parallel to the fcc-Ni (γ-phase) (111)-interface.

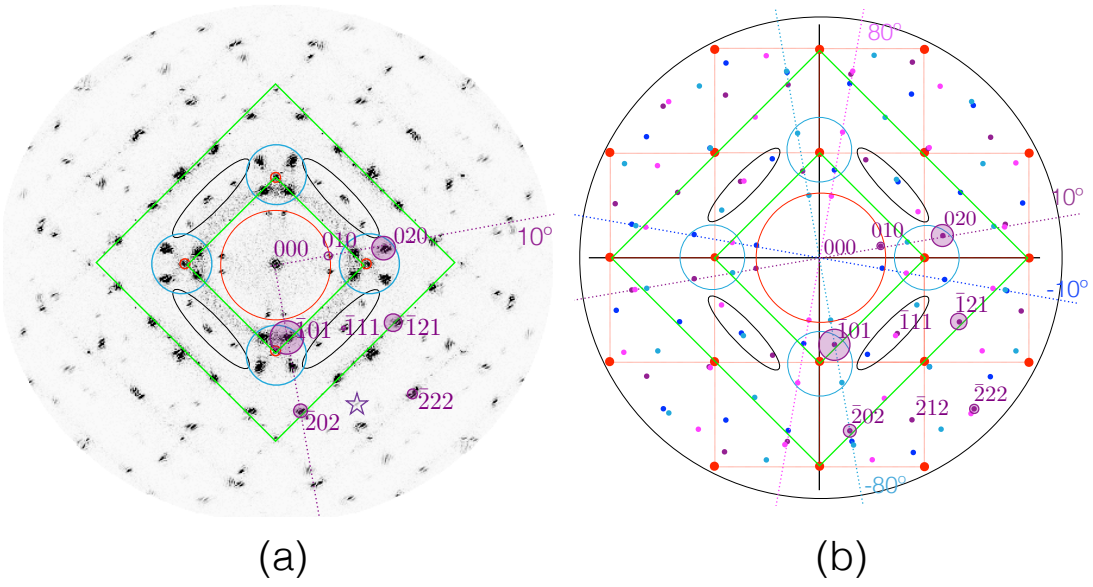

Figure 10: (a) Virtual SAED pattern for a section of the system in the z direction from $z = 65$ to 105 $\mathring{A}$. (b) Overlay of the calculated diffraction pattern of the Ni-[001] substrate and four orientations of NiAl-[101]. Red bullet points are Ni peaks. The red square lattice corresponds to the Ni reciprocal lattice. Dark blue, light blue, cyan, and magenta point bullets are NiAl peaks. Each color corresponds to one of the four orientations indicated by the dashed lines. As a guide for visualization, groups of peaks are encircled in both (a) and (b). The intensity threshold of the peak (000) is bounded intentionally. (For interpretation of the reference to color in this figure legend, the reader is referred to the web version of this article.)

In each plane, small NiAl clusters form, separated by grain boundaries. If the orientation of a grain is defined as the orientation of its closest neighbors (β-angle), three main orientations were observed, as shown in Fig. 6b. Nevertheless, a weak degeneracy of the left peak was detected.

Given the hexagonal arrangement of Ni at the interface, a 2D NiAl (101)-unit cell can easily be constructed on a 2D Ni (111)-unit cell as shown in Fig. 11. Note that the relation (4) implies that the diagonal ℓ_γ of the 2D hexagonal (111)-unit cell is equal to the diagonal ℓ_α of the 2D rectangular (101)-unit cell. Six different choices options are possible for the alignment of the α-diagonal on a γ-diagonal: $(101)_\gamma$ $(10\bar{1})_\gamma$ $(110)_\gamma$ $(1\bar{1}0)_\gamma$ $(101)_\gamma$ or $(01\bar{1})_\gamma$. During the nucleation process, the central Ni atom may be replaced by an Al atom. This substitution seems possible from an energetic point of view because the distance $\ell_\gamma/2$ between the nearest neighbor Ni atoms on the diagonal in the γ-phase is the same as for the Ni and Al atoms in the α-phase. The hexagonal γ-cell is inscribed in a circle of diameter ℓ_γ. For any point P on this circle, $\widehat{APD}$ is a rectangle triangle, if A and D are vertices of the hexagon located on the same diagonal. If P is located at a distance a_α from A, the triangle $\widehat{APD}$ and its symmetrical with respect to the diagonal form a rectangular 2D α-cell in a (011)-plane. A slight displacement of Ni atoms is sufficient to obtain this cell (Fig. 11a). Six different choices options are possible: by

choosing the other point P on the large circle at a distance a_α from the A intersection between the two circles (Fig. 11b), or by performing the same operation on the other two diagonals (Figs. 11c-11f).

The orientation of the $(011)_\alpha$ phase is defined, as previously, by the angle between the direction of the nearest neighbors of the same species and the horizontal axis (2D-polar angle). The six orientations observed can be grouped into pairs of similar orientation (e.g. 55° and 64°), leaving only three main orientations (see Fig.6b). The diagonals of the hexagonal 2D unit cells show three orientations: $\pi/3$, $2\pi/3$ and π. The orientation of diagonal of the 2D rectangular α-cell is $\arcsin\sqrt{2/3} = 55°$ or $\arcsin\sqrt{1/3} = 35°$, depending on whether the rectangle is positioned on its smaller (a_α) or larger ($\sqrt{2}a_\alpha$) side. To align the diagonal of the α-cell and the $\pi/3$-diagonal of the γ-cell, a rotation of $\pi/3 - \arcsin\sqrt{2/3} = 5°$ or $\pi/3 - \arcsin\sqrt{1/3} = 25°$ is necessary (see Figs. 11f and 11e).

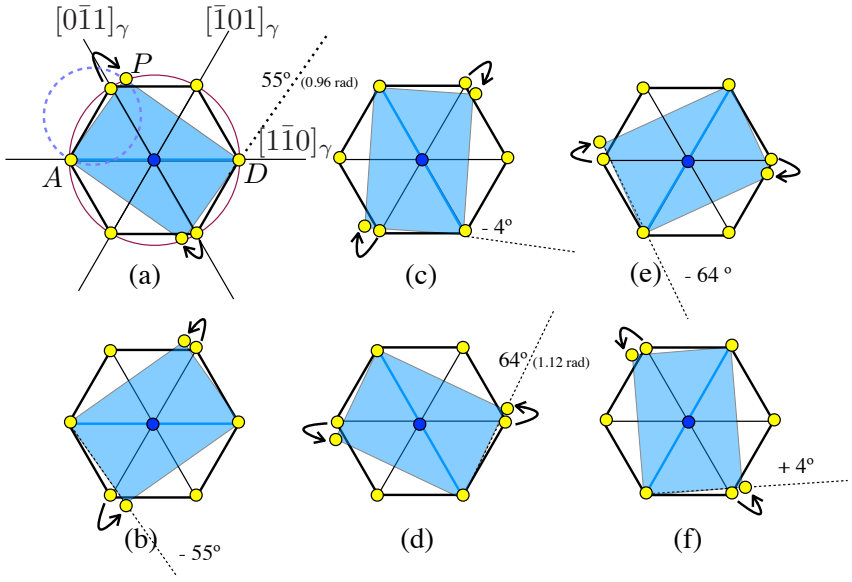

Figure 11: The six orientations of the 2D α-cell with respect to the 2D γ-cell. The hexagonal γ-cell is represented in black, while the rectangular α-cell is in blue. The central atom (located in 0) is a Ni atom in the γ-cell and an Al atom in the α-cell. The orientation angle β of the NiAl cell is defined as the angle between the direction (dotted line) of nearest neighbors of the same species (here Ni atoms), and the x-axis (horizontal). The value of β is provided for each orientation. For interpretation of the reference to color in this figure legend, the reader is referred to the web version of this article.

The $\alpha-$ and $\gamma-$ lattices are linked by the following orientation relationship:

$$[111]_\gamma \parallel [011]_\alpha \tag{8a}$$
$$[\bar{1}01]_\gamma \parallel [\bar{1}\bar{1}1]_\alpha \tag{8b}$$
$$[1\bar{2}1]_\gamma \parallel [2\bar{1}1]_\alpha \tag{8c}$$

In the plane $(011)_\alpha$, the direction $[\bar{1}\bar{1}1]_\alpha$ corresponds to one diagonal of the 2D α-cell. The relation (8b) corresponds to the alignment of $[\bar{1}\bar{1}1]_\alpha$ with the diagonal of the hexagon $[\bar{1}0\bar{1}]_\gamma$. The other two possibilities are: $[0\bar{1}1]_\gamma$ and $[1\bar{1}0]_\gamma$. The orientation relation (8) corresponds to the Kurdjumov and Sachs (K-S) orientation [25].

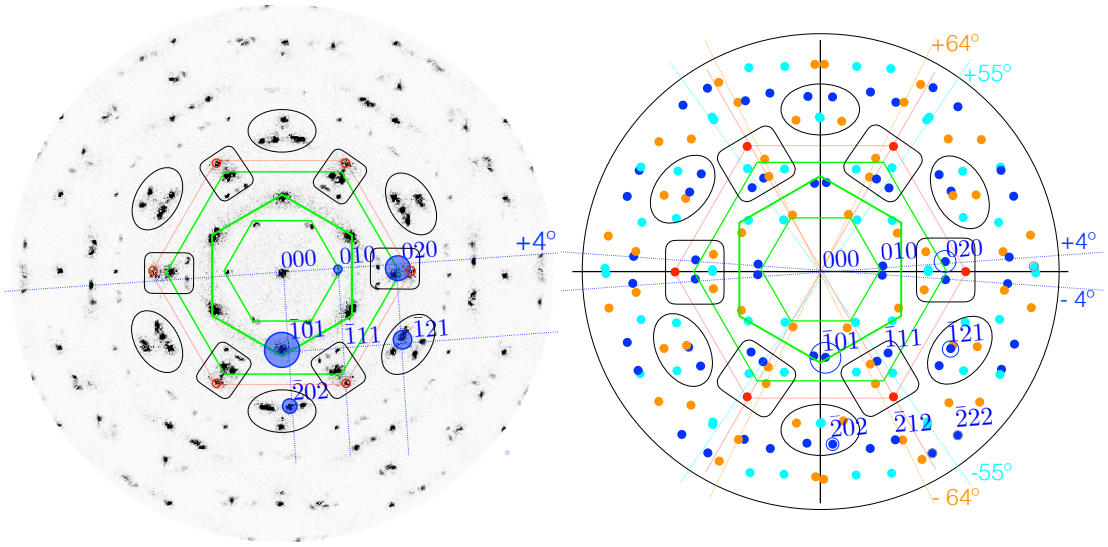

Figure 12: (a) Virtual SAED pattern for a section of the system in the z direction from $z = 65$ to $105\,\mathring{A}$. (b) Overlay of the calculated diffraction pattern of the Ni-[111] substrate and six orientations of NiAl-[101]. Red bullet points are Ni peaks. Blue, cyan, and orange bullet points are NiAl peaks corresponding to $\pm4°$, $\pm55°$, and $\pm64°$ orientations. The orientations are indicated by the dashed lines. As a guide for visualization, groups of peaks are encircled in both (a) and (b). The intensity threshold of the peak (000) is bounded intentionally. (For interpretation of the reference to color in this figure legend, the reader is referred to the web version of this article.)

We performed a diffraction analysis in this case, in the same way as in the previous section. The simulated and theoretical results are depicted in Fig. 12. The complex SAED pattern can easily be interpreted using the calculated diffraction pattern. The calculated diffraction pattern is the overlay of the six disoriented NiAl-[101] on Ni-[111]. Each NiAl-[101] pattern, similar to the one presented in Fig. 9c, was rotated by $\pm4°$, $\pm55°$, and $\pm64°$. The red hexagonal lattice corresponds to the Ni reciprocal lattice shown in Fig. 12a. The green hexagons are related to the (010), $(\bar{1}01)$, and (020) diffraction planes of NiAl. The typical hexagonal arrangement of Ni-[111] is found in the diffraction pattern both for Ni peaks (red bullet points in Fig. 12a) and NiAl peaks (green hexagons in Fig. 12a). Similar clusters of peaks are obtained in both cases.

3.3 Ni-substrate in orientation (110)

We now consider the case of a Ni interface with an orientation (110). As depicted in Fig. 3c, the Ni atoms are closely aligned in one direction and separated by a_γ in the other direction. The atoms located in the plane below are shifted by $a_\gamma/2$. Formation of the intermetallic phase was observed, but different in appearance from the two previous situations. The growth of NiAl did not occur in planes parallel to the interface. Tilted grains were imbricated and formed a large crystallized zone with a specific microstructure, as shown in Fig. 13.

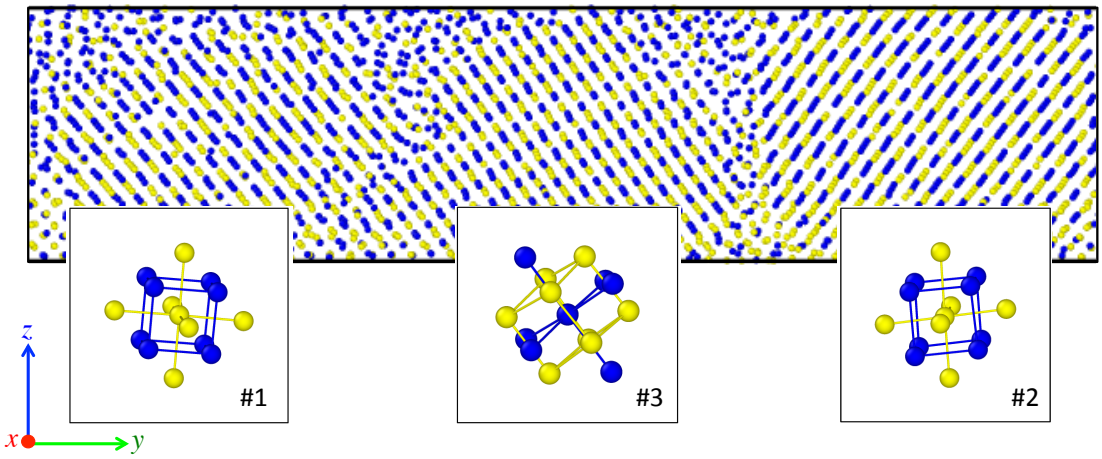

Figure 13: Snapshot of the crystallized zone formed on the Ni (110)-interface. This is the y-z view of a section along x. The Al and Ni atoms are shown as blue and yellow spheres, respectively. Insets correspond to the orientation of NiAl in the grains. For interpretation of the reference to color in this figure legend, the reader is referred to the web version of this article.

We here describe the structure of the polycrystalline $B2$-NiAl phase observed in the simulations. The structure is given by the grain orientation with respect to the sample (for a detailed description see [26]). This is expressed as follows:

$$K_{\text{grain}} = g\, K_{\text{sample}} \tag{9}$$

where $K_{\text{grain}} = \{\vec{e_1}, \vec{e_2}, \vec{e_3}\}$ and $K_{\text{sample}}\{\vec{1_x}, \vec{1_y}, \vec{1_z}\}$ are the crystal and sample coordinate systems, respectively, and g is the orientation matrix, that embodies the rotation of the sample coordinates on the crystal (grain) coordinates. As shown in Fig. 13, three grains were observed, each with a given orientation. For the grain located in the middle of the sample, the orientation matrix averaged over all the atoms belonging to the grain reads:

$$g_{\text{g}\#3} = \begin{pmatrix} -0.68 & 0.54 & 0.48 \\ -0.72 & -0.6 & -0.36 \\ 0.08 & -0.6 & 0.796 \end{pmatrix} \approx (1\bar{1}2)[\bar{1}\bar{1}0] \tag{10}$$

For the grains located to the left and to the right of the sample, the orientation reads:

$$g_{\mathrm{g}\#1} = \begin{pmatrix} 0.1424 & 0.9491 & 0.0818 \\ -0.9269 & 0.1261 & 0.1198 \\ 0.1195 & -0.0882 & 0.9619 \end{pmatrix} \approx (001)[0\bar{1}0] \tag{11}$$

and

$$g_{\mathrm{g}\#2} = \begin{pmatrix} 0.8351 & 0.2370 & -0.1346 \\ -0.2224 & 0.8121 & -0.0472 \\ 0.1089 & 0.0686 & 0.9316 \end{pmatrix} \approx (001)[100] \tag{12}$$

These orientations are very similar. Grains #1 and #2 differ only by a slight shift in the direction d_3.

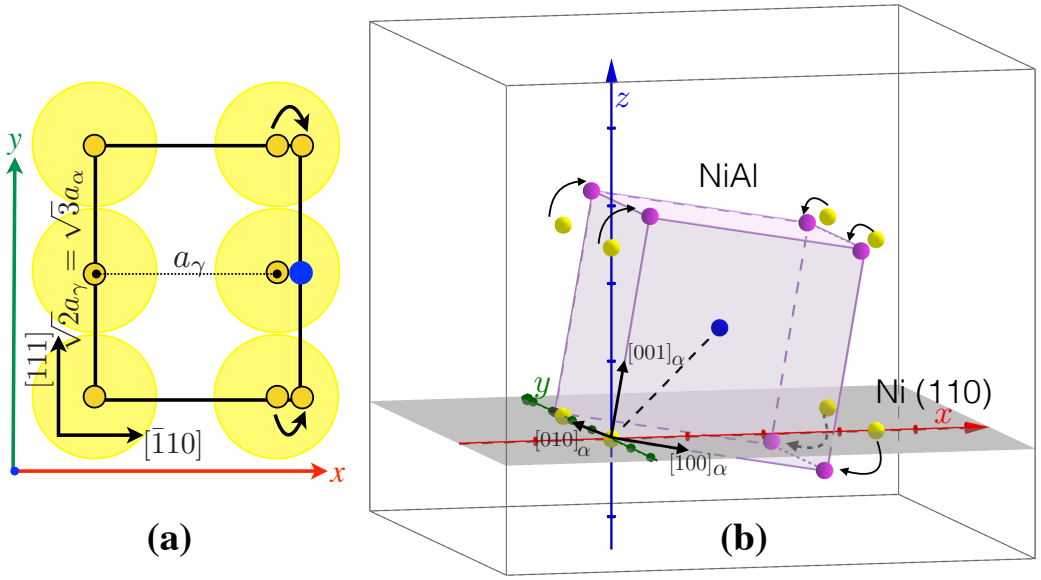

Figure 14: Schematic representation of the epitaxial relationship in the case of NiAl on Ni (110).

The orientation of grain #3 is easy to reconstruct, using simple geometry. Let us consider the (110) plane of Ni at the interface. The alignment of Ni atoms is given in Fig. 14a. On a [111]-row, the distance ℓ_γ between 3 Ni-neighbors is equal to the diagonal of the NiAl cell ℓ_α. If we suppose that one Al atom replaces one Ni atom, the configuration is favorable to the formation of a 2D unit cell in the orientation (112). A displacement of the atoms gives the expected cell, provided another Al atom replaces another Ni atom on the same $[\bar{1}10]$ row. A displacement of 15% is necessary to form the α-phase. A slice perpendicular to z shows alternating rows of Ni and Al atoms. These rows are separated by a distance of $\sqrt{2}a_\alpha$, while the distance between atoms is $\sqrt{3}a_\alpha/2$. This feature induces stress and defects that may alter the configuration.

The orientation of grains #1 and #2 is obtained in the same way. Let us suppose that one Al atom replaces a Ni atom in the upper plane, where atoms are slightly shifted

(see Fig. 3c). With a slight displacement of Ni atoms in the reference plane and in the next plane above that, a unit cell of NiAl is laid on a (110) Ni interface, as shown in Fig. 14b. The direction $[010]_\alpha$ is aligned with the direction $[010]_\gamma$. The direction $d_3 = [001]_\alpha$ is slightly inclined with respect to $[001]_\gamma$.

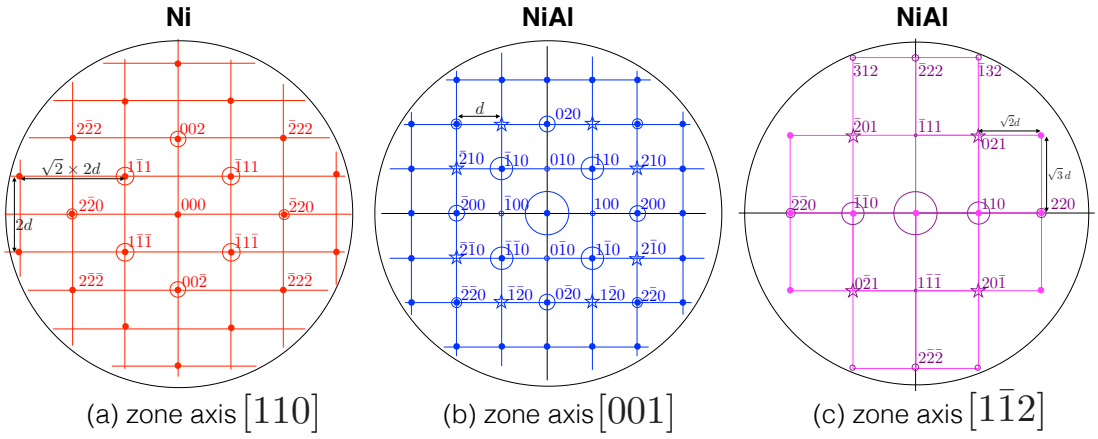

Figure 15: (a) Calculated diffraction pattern of fcc-Ni substrate with zone axis aligned along the [110]-direction. The distance d is $1/a_\gamma$. (b)-(c) Calculated diffraction pattern of bcc-NiAl with zone axis aligned along the [001]- and [1$\bar{1}$2]-directions. The distance d is $1/a_\alpha$. Representative points are labeled by the plane of diffraction they refer to. Each bullet point is surrounded by a circle corresponding to the intensity of the peak of diffraction. Stars correspond to very weak peaks.

We also performed a diffraction analysis. Fig. 15a depicts the calculated diffraction pattern of fcc-Ni with zone axis along the [100]-direction of the solid Ni substrate in Fig. 3c. Figures 15b-c represent the calculated diffraction patterns of NiAl with growth along the zone axis observed in the simulations (see eqs. (10)-(12)). Figure 16b is the overlay of Figs. 15a, 15b, and 15c. The characteristic rectangular unit cell $2d \times \sqrt{2}\,2d$ (in red) drawn by peaks of the fcc-(110)-plane in the reciprocal lattice is observed in the virtual SAED pattern in Fig. 15a. There is noticeable similarity between the simulated 16a and calculated 16a SAED patterns. More intense peaks are grouped in recognizable entities. Despite the complexity of the polycrystalline $B2$-NiAl phase observed in the simulations, the diffraction pattern looks simple, due to the limited orientations in the texture.

3.4 Nucleation and growth

The previous analysis (see sections 3.1 and 3.2) is applied to each atom belonging to the bcc phase. The bcc atoms are then colored according to the local orientation of the grain they belong to. Figure 17 shows the lower half of the system. At $t = 2$ ns, a spontaneous nucleation of small clusters of bcc atoms was observed close to the interface. Until $t = 4$ ns, lateral growth occurred. At $t = 6$ ns, almost all the regions close

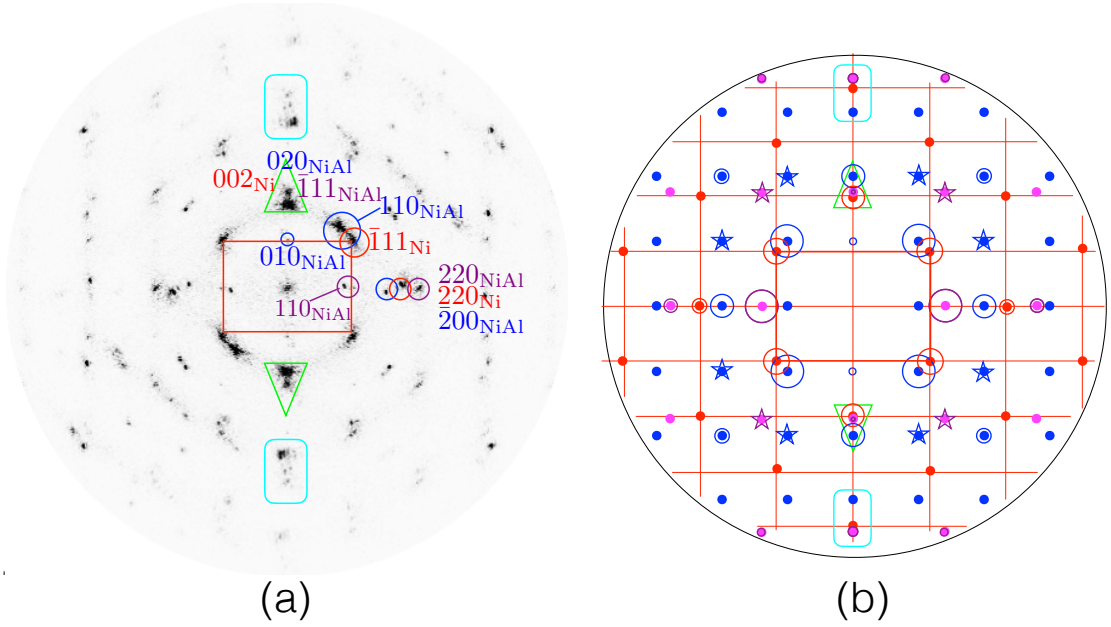

Figure 16: (a) Virtual SAED pattern for a section of the system in the z direction from $z = 65$ to 105 $\mathring{A}$. (b) Overlay of the calculated diffraction pattern of the Ni-[110] substrate and crystallized NiAl grains. Red bullet points are Ni peaks. The red square lattice corresponds to the Ni reciprocal lattice. Blue and magenta bullet points are NiAl peaks. As a guide for visualization, groups of peaks are encircled in both (a) and (b). The intensity threshold of the peak (000) is bounded intentionally. (For interpretation of the reference to color in this figure legend, the reader is referred to the web version of this article.)

to the interface were covered by bcc atoms. These atoms belong to disoriented grains, separated by thin amorphous or liquid zones. From 6 ns to 20 ns, the vertical growth of the grains is due to the precipitation of Ni and Al from the liquid Al+Ni solution. Due to precipitation, the number of Ni atoms in the melt decreased. But this decrease in Ni atoms was compensated by the diffusion of Ni from the solid layer through the inter-grain channels. A stationary gradient of Ni from the solid layer to the inner layer was established throughout the process, explaining the limited crystallization in the upper planes, and the specific morphology of the grains (see also Fig. 2).

It is interesting to follow the atomic organization (arrangement) in planes on both sides of the interface, at different times during the reactive process. Fig.18a shows an atomic layer of solid fcc Ni in the orientation (111), close to the Ni-Al interface. After the melting of Al, Ni starts to dissolve in the inner liquid layer. Most of the vacancies thus created are occupied by incoming Al atoms. The small hexagons that are formed by an Al atom surrounded by Ni atoms correspond to the early formation of (110)-NiAl seeds, after replacement of a Ni atom by an Al atom. This is exactly the mechanism depicted in Fig. 11. In the crystallized inner layer, atomic planes paral-

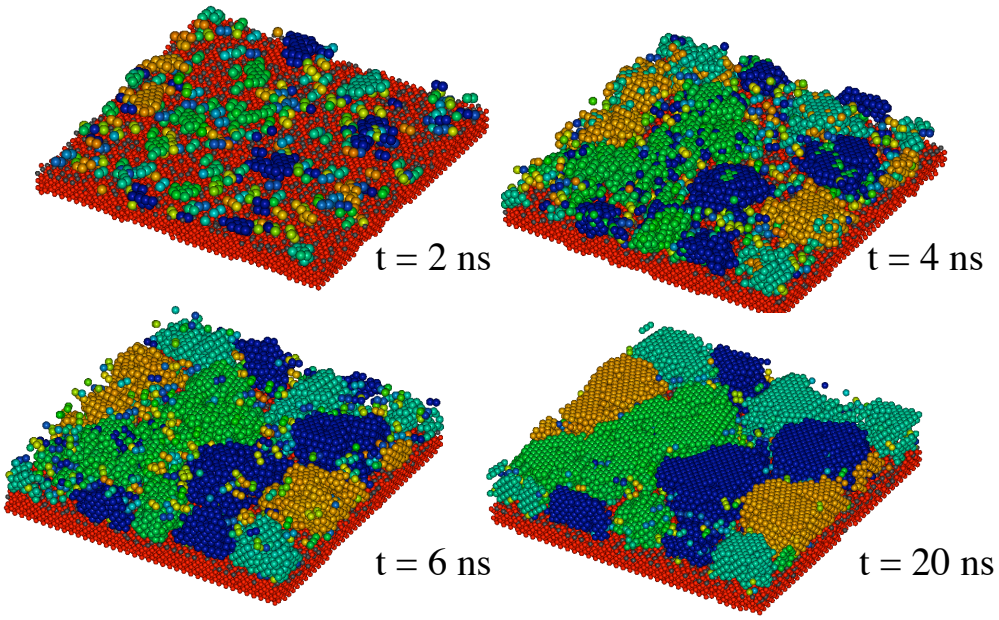

Figure 17: Snapshots of the system at different times during the nucleation and growth process. The bcc atoms are colored in orange, cyan, green and blue, according to their local orientation (angle β). The fcc atoms are represented as small red and grey spheres, depending on their chemical nature. Only the lower part of the system has been represented.

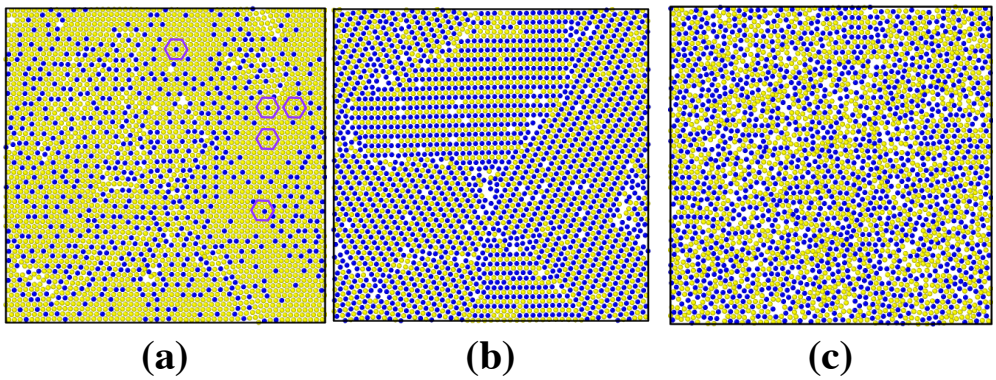

Figure 18: (a) Snapshot of a system slice just below the interface, immediately after the start of the mixing process. (b) Snapshot of a slice above the interface, after crystallization of the NiAl phase ($t = 40$ ns). (c) Snapshot of a slice in the liquid region above the crystallized region.

lel to the interface are covered by Ni and Al atoms in equal proportions, as shown in Fig. 18b. The atomic plane shows alternating lines of Ni and Al arranged in regions with different orientations. As expected, the atomic arrangement is characteristic of the (110) orientation of NiAl. Fig. 18c gives an instantaneous image of the arrangement of Ni and Al atoms in the liquid inner layer, before crystallization starts ($t < 2$ns). Only

a small number of organized regions are detectable. All other atoms are randomly mixed.

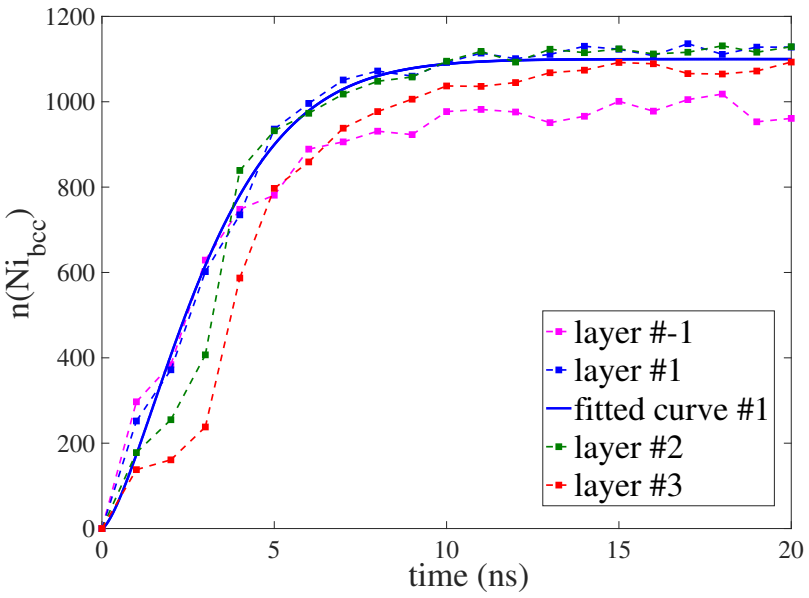

Figure 19: Number of Ni atoms in local bcc configuration in three different layers close to the interface versus time.

In order to understand the crystal growth mechanism of the NiAl phase, the coverage of the atomic planes by bcc Ni atoms was tracked for the (001)-Ni orientation, as shown in Fig. 19. This study was carried out in analogy to crystal growth during film deposition. The layers correspond to the atomic planes parallel to the interface: the layer $\# - 1$ is located below the interface; the layers #1, #2, and #3 are the successive atomic planes just above the interface. The number of bcc Ni atoms grows simultaneously in layers $\# - 1$ and #1. Coverage reaches almost 80% in layer #1 but never exceeds 60% in layer $\# - 1$. Layer #2 starts to be covered by bcc Ni before layer #1 has reached its plateau value. The same behavior is observed for layer #3. Upper layers start to be arranged in bcc orientation before the bcc coverage of lower planes is completed. This proves that the crystal growth here is not a 2D layer-by-layer crystallization.

The first overlay coverage C_1 can be analytically expressed as [27]:

$$C_1(t) = C\,[1 - \exp(-t^m/\tau^m)] \tag{13}$$

where C is a normalization factor, and τ a characteristic time. According to the literature, the fit parameter $m = 3$ corresponds to a pure nucleation and growth mechanism, and $m = 1$ to a pure continuous growth mechanism. In our case, we obtain $m = 1.45$ which means that the growth mechanism is intermediate between purely nucleated and purely continuous. All these analyses give concordant information about the nature of the crystal growth kinetics. We also studied the influence of the orientation of the

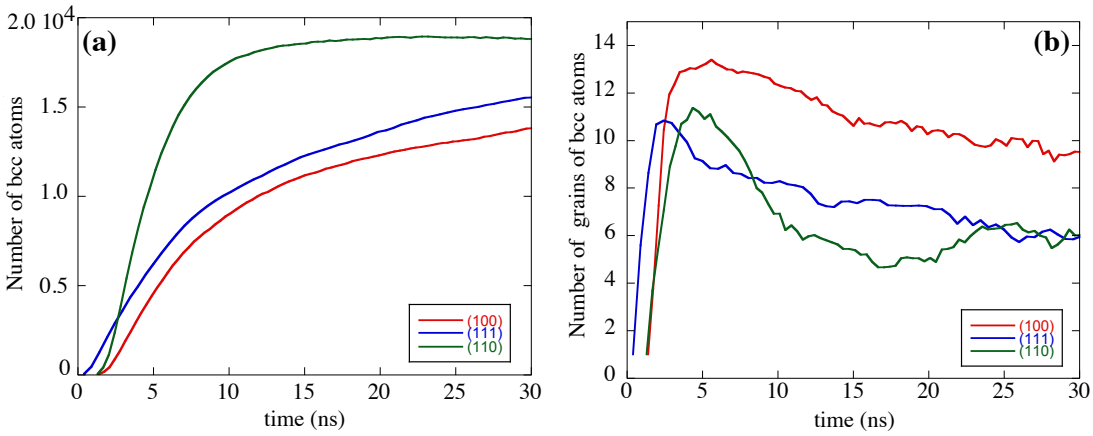

Figure 20: (a) Number of bcc atoms at the lower interface as a function of time for the three orientations of the interface. (b) Number of grains of bcc atoms at the interface as a function of time.

Ni-substrate on nucleation and growth. Fig. 20a shows the evolution of the number of bcc atoms (Ni and Al atoms) in the lower half of the inner layer. The greatest coverage was observed for the (101)-orientation. The delay in the start of nucleation is slightly shifted but the growth rate is very steep. High coverage is reached in a very short time. In the case of the (111)-orientation, nucleation starts very rapidly and growth continues throughout the simulation (up to 40 ns). A similar behavior is observed in the case of the (001)-orientation, but the total number of bcc atoms remains lower than in the (111)-orientation. The 3D morphology observed for the (101)-orientation promotes crystallization in comparison with the mosaic precipitation that occurs layer by layer. Crystallization starts sooner on the (111) surface, because of its lower surface energy: $E^{\mathrm{fcc}}_{111} < E^{\mathrm{fcc}}_{001} < E^{\mathrm{fcc}}_{110}$.

The number of grains was tracked as a function of time, for the three orientations. A cluster of atoms is defined as a set of connected bcc atoms. If the number of atoms in a cluster is greater than 20, the cluster is counted as a grain. The number of grains is quite large at the early stage, reflecting the appearance of local rearrangements of Ni and Al atoms, leading to a stable nucleus (see also Fig. 17 at $t = 2$ ns). Next, the number of grains decreases as a function of time, due to coalescence of contiguous grains with the same orientation. Small grains may dissolve, and the atoms thus released will precipitate on other grains. The number of grains remains greater in the case of (001)-Ni than in the two other cases, due to the existence of four possible orientations that forbid easy coalescence. In the case of the (111)-Ni orientation, there are three main orientations, which are formed of three slightly different pairs. This situation is more favorable to coalescence. Finally, in the case of the (101)-Ni orientation, the number of grains is less stable, probably due to a reorganization in tilted grains.

4 Conclusions

Self-propagating high-temperature synthesis in Ni-Al nanofoils results in the formation of NiAl at interfaces. From the melting temperature of Al, the reaction is associated with a mixing stage (Ni into liquid Al) followed by alloying between metals (precipitation and crystallization). This leads to a specific microstructure along the foil. The new phase appears as many nuclei at interfaces between the solid Ni layers and the liquid alloy. Grain growth is due to the precipitation of Ni and Al present in the inner layer. The resulting microstructure is a set of disoriented grains, separated by grain boundaries. These features are typical of samples with an excess of Ni, where nucleation is observed at the solid-liquid interfaces. In this work, the important issue of orientation control was addressed.

We considered the solid Ni interface with characteristic low-index orientations. For the (001) and (111) Ni-orientations, the NiAl grains were formed in (101) planes, parallel to the interface. This observation is coherent with the relative stability of the surfaces in NiAl: $E^{\mathrm{bcc}}_{110} < E^{\mathrm{bcc}}_{100} < E^{\mathrm{bcc}}_{111}$. Their growth results from competition between the layer covering (2D) and precipitation from the melt (3D), and follows a typical Stranski-Krastanov mechanism. The NiAl phase grows epitaxially on the Ni substrate. In the case of the (001) Ni-orientation, four orientations of NiAl grains are observed by MD simulations and obtained by epitaxial relationships. This corresponds to the epitaxy between the bcc and fcc phases given by the Pitsch transformation. In the case of the close-packed (111) Ni-orientation, six orientations, grouped into three similar pairs, were predicted by epitaxial relationships. The Kurdjumov and Sachs (K-S) orientation between bcc and fcc was observed. Besides the analysis of MD results, we provide the full expression of the transformations and give a simple geometric interpretation of the observations.

In the case of a (101) Ni-orientation, the situation is more complex. The NiAl grains do not have the characteristic rounded shape, and they invade the entire inner layer. The NiAl planes are not parallel to the Ni interface. Nevertheless, we provide the orientation matrix describing the texture, and derive the topotaxial relationships using simple geometric considerations.

Finally, we have shown that the orientation of the Ni substrate plays an important role in nucleation and growth.

Specific tools dedicated to texture analysis of the product were also developed and used to characterize NiAl intermetallic grains. More generally, these tools can be used to map the crystallographic orientations of the phase formed during MD simulations.

Acknowledgments
The use of computational facilities at the Computing Center of the University of Burgundy, PSIUN-CCUB, is gratefully acknowledged. Fruitful discussions with Dr. R. Chassagnon were of great help with diffraction analysis.

A Appendix

This appendix gives the explicit derivation of the orientations in the case of NiAl-(101) on Ni-(001) and Ni-(111). We first consider the case of NiAl-(101) on Ni-(001). Relationships (5) only concern parallelisms between vectors in the two lattices. In order to find the coordinate transformation $(\alpha J \gamma)$, it is necessary to ensure that the parallel vectors are also equal, since the magnitude must remain invariant to a coordinate transformation. The constants k, g and m are defined as

$$k = \pm \frac{|[001]_\gamma|}{|[101]_\alpha|} = \pm \frac{\sqrt{2}}{2}\, a \tag{14a}$$

$$g = \pm \frac{|[\bar{1}10]_\gamma|}{|[12\bar{1}]_\alpha|} = \pm \frac{\sqrt{3}}{3}\, a \tag{14b}$$

$$m = \pm \frac{|[110]_\gamma|}{|[\bar{1}10]_\alpha|} = \pm \sqrt{\frac{2}{3}}\, a \tag{14c}$$

where a denotes the ratio between lattice parameters $a = a_\gamma / a_\alpha = \sqrt{3/2}$. The transformation from one basis to the other is given by:

$$[k\,0\,k]_\alpha = (\alpha J \gamma)\,[001]_\gamma \tag{15a}$$

$$[g\,2g\,\bar{g}]_\alpha = (\alpha J \gamma)\,[\bar{1}10]_\gamma \tag{15b}$$

$$[\bar{m}\,m\,m]_\alpha = (\alpha J \gamma)\,[110]_\gamma \tag{15c}$$

which reads, in matrix form:

$$\begin{pmatrix} k & g & \bar{m} \\ 0 & 2g & m \\ k & \bar{g} & m \end{pmatrix} = (\alpha J \gamma) \begin{pmatrix} 0 & \bar{1} & 1 \\ 0 & 1 & 1 \\ 1 & 0 & 0 \end{pmatrix} \tag{16}$$

and

$$(\alpha J \gamma) = a\, \frac{1}{2} \begin{pmatrix} -g-m & g-m & 2k \\ -2g+m & 2g+m & 0 \\ g+m & -g+m & 2k \end{pmatrix} \equiv a \cdot H \tag{17}$$

The factor a corresponds to strain along the axis (dilation).

The matrix $(\alpha J \gamma)$ has the form of a matrix product $R_y(\theta) \cdot R_z(\varphi)$:

$$\begin{aligned} R = R_y(\theta) \cdot R_z(\varphi) &= \begin{pmatrix} \cos\theta & 0 & \sin\theta \\ 0 & 1 & 0 \\ -\sin\theta & 0 & \cos\theta \end{pmatrix} \begin{pmatrix} \cos\varphi & -\sin\varphi & 0 \\ \sin\varphi & \cos\varphi & 0 \\ 0 & 0 & 1 \end{pmatrix} \\ &= \begin{pmatrix} \cos\theta\cos\varphi & -\cos\theta\sin\varphi & \sin\theta \\ \sin\varphi & \cos\varphi & 0 \\ -\sin\theta\cos\varphi & \sin\theta\sin\varphi & \cos\theta \end{pmatrix} \end{aligned} \tag{18}$$

γ-cell diagonal	k/a	g/a	m/a	θ	φ
$[110]_\gamma$	$\sqrt{2}/2$	$-1/\sqrt{3}$	$\sqrt{2/3}$	$\pi/4$	$1.7407\,(100°)$
$[110]_\gamma$	$-\sqrt{2}/2$	$1/\sqrt{3}$	$\sqrt{2/3}$	$-3\pi/4$	$-0.1699\,(-9.74°)$
$[\bar{1}10]_\gamma$	$\sqrt{2}/2$	$-1/\sqrt{3}$	$\sqrt{2/3}$	$\pi/4$	$0.1699\,(9.74°)$
$[\bar{1}10]_\gamma$	$-\sqrt{2}/2$	$-1/\sqrt{3}$	$-\sqrt{2/3}$	$-3\pi/4$	$1.4001\,(80°)$

Table 2: Coordinate transformation $(\alpha J\gamma)$ for the two diagonals of the γ square unit cell. The orientation $[\bar{1}11]_\alpha$ of the diagonal of the NiAl cell remains fixed. Euler angles θ and φ correspond to a rotation $R_y(\theta)\cdot R_z(\varphi)$.

The coordinate transformation (17) is strictly equivalent to the above rotation (18) if the matrices H and R are identical term by term. The results are summarized in Table 2. The relationships (14) for the constants k, g and m are found and the angles of rotation are determined.

We now consider the case of NiAl-(101) on Ni-(111). The relationships (8) only concern the parallelism between vectors in the two lattices. In order to find the coordinate transformation $(\alpha J\gamma)$, it is necessary to ensure that the parallel vectors are also equal, since the magnitude must remain invariant to a coordinate transformation. The constants k, g and m are defined as:

$$k = \pm\frac{|[111]_\gamma}{|[011]_\alpha|} = \pm\sqrt{\frac{3}{2}}\,a \tag{19a}$$

$$g = \pm\frac{|[\bar{1}01]_\gamma|}{|[\bar{1}\bar{1}1]_\alpha|} = \pm\sqrt{\frac{2}{3}}\,a \tag{19b}$$

$$m = \pm\frac{|[1\bar{2}1]_\gamma}{|[2\bar{1}1]_\alpha|} = \pm\,a \tag{19c}$$

The transformation from one basis to the other is given by:

$$[0\ k\ k]_\alpha \;= (\alpha J\gamma)\,[111]_\gamma \tag{20a}$$

$$[\bar{g}\ \bar{g}\ g]_\alpha \;= (\alpha J\gamma)\,[\bar{1}01]_\gamma \tag{20b}$$

$$[2m\ \bar{m}\ m]_\alpha \;= (\alpha J\gamma)\,[1\bar{2}1]_\gamma \tag{20c}$$

which reads, in the matrix form:

$$\begin{pmatrix} 0 & \bar{g} & 2m \\ k & \bar{g} & \bar{m} \\ k & g & m \end{pmatrix} = (\alpha J\gamma) \begin{pmatrix} 1 & \bar{1} & 1 \\ 1 & 0 & \bar{2} \\ 1 & 1 & 1 \end{pmatrix} \tag{21}$$

$$(\alpha J\gamma) = a \begin{pmatrix} \frac{1}{2}g + \frac{1}{3}m & -\frac{2}{3}m & -\frac{1}{2}g + \frac{1}{3}m \\ \frac{1}{3}k + \frac{1}{2}g - \frac{1}{6}m & \frac{1}{3}k + \frac{1}{3}m & \frac{1}{3}k - \frac{1}{2}g - \frac{1}{6}m \\ \frac{1}{3}k - \frac{1}{2}g + \frac{1}{6}m & \frac{1}{3}k - \frac{1}{3}m & \frac{1}{3}k + \frac{1}{2}g + \frac{1}{6}m \end{pmatrix} \equiv a\cdot H \tag{22}$$

The matrix $(\alpha J\gamma)$ has the form of a matrix product $R_z(\psi)\cdot R_y(\theta)\cdot R_z(\varphi)$.

$$R = R_x(\psi)\cdot R_y(\theta)\cdot R_z(\varphi) = \begin{pmatrix} 1 & 0 & 0 \\ 0 & \cos\psi & -\sin\psi \\ 0 & \sin\psi & \cos\psi \end{pmatrix} \begin{pmatrix} \cos\theta & 0 & \sin\theta \\ 0 & 1 & 0 \\ -\sin\theta & 0 & \cos\theta \end{pmatrix} \begin{pmatrix} \cos\varphi & -\sin\varphi & 0 \\ \sin\varphi & \cos\varphi & 0 \\ 0 & 0 & 1 \end{pmatrix}$$
$$= \begin{pmatrix} \cos\theta\cos\varphi & -\cos\theta\sin\varphi & \sin\theta \\ \sin\psi\sin\theta\cos\varphi+\cos\psi\sin\varphi & -\sin\psi\sin\theta\sin\varphi+\cos\psi\cos\varphi & -\sin\psi\cos\theta \\ -\cos\psi\sin\theta\cos\varphi+\sin\psi\sin\varphi & \cos\psi\sin\theta\sin\varphi+\sin\psi\cos\varphi & \cos\psi\cos\theta \end{pmatrix} \quad (23)$$

The coordinate transformation (22) is strictly equivalent to the above rotation (23), if the matrices H and R are identical term by term. The results are given in Table 3.

	k/a	g/a	m/a	θ	φ	ψ
$[\bar{1}01]_\gamma \parallel [\bar{1}\bar{1}1]_\alpha$	$\sqrt{3/2}$	$\sqrt{2/3}$	1	$-0.074985\,(-4°)$	$0.732251\,(42°)$	$0.167924\,(10°)$
$[\bar{1}01]_\gamma \parallel [\bar{1}\bar{1}1]_\alpha$	$\sqrt{3/2}$	$-\sqrt{2/3}$	-1	$3.066607\,(176°)$	$0.732251\,(42°)$	$1.402872\,(80°)$
$[0\bar{1}1]_\gamma \parallel [\bar{1}\bar{1}1]_\alpha$	$\sqrt{3/2}$	$-\sqrt{2/3}$	1	$0.835425\,(48°)$	$3.02969\,(174°)$	$-1.319731\,(-76°)$
$[0\bar{1}1]_\gamma \parallel [\bar{1}\bar{1}1]_\alpha$	$\sqrt{3/2}$	$\sqrt{2/3}$	-1	$-2.306168\,(-132°)$	$3.02969\,(174°)$	$2.890527\,(166°)$
$[1\bar{1}0]_\gamma \parallel [\bar{1}\bar{1}1]_\alpha$	$-\sqrt{3/2}$	$-\sqrt{2/3}$	1	$-0.729728\,(-41°)$	$0.100679\,(-6°)$	$3.040913\,(174°)$
$[1\bar{1}0]_\gamma \parallel [\bar{1}\bar{1}1]_\alpha$	$\sqrt{3/2}$	$-\sqrt{2/3}$	-1	$2.411865\,(138°)$	$-1.671475\,(96°)$	$3.040913\,(174°)$

Table 3: Coordinate transformation $(\alpha J\gamma)$ for the three diagonals of the γ hexagonal unit cell, given the orientation $[\bar{1}\bar{1}1]_\alpha$ of the diagonal of the NiAl cell. For information, the associated Euler angles are given, corresponding to a rotation $R_x(\psi)\cdot R_y(\theta)\cdot R_z(\varphi)$.

The orientation (8b) corresponds to one diagonal of the hexagon. Two other options are possible: $[0\bar{1}1]_\gamma$ and $[1\bar{1}0]_\gamma$. In each case, it is easy to compute the values of k, g and m, together with the corresponding Euler angles (see Table 3). The degenerescence for the 6 orientations predicted by the simple geometric construction is recovered.

References

[1] T.W. Barbee and T. Weihs, U.S. Patent N 5538795, Ignitable heterogeneous stratified structure for the propagating of an internal exothermic chemical reaction along an expanding wavefront and method of making same, July 23 (1996)

[2] J. Wang, E. Besnoin, A. Duckham, S. J. Spey, M. E. Reiss, O. M. Knio, and T. P. Weihs, Joining of stainless-steel specimens with nanostructured Al/Ni foils, J. Appl. Phys. 95 (2004) 248-256 doi: 10.1063/1.1629390

[3] X. Zhou, M. Torabi, J. Lu, R. Shen and K. Zhang, Nanostructured Energetic Composites: Synthesis, Ignition/Combustion Modeling, and Applications, ACS Appl. Mater. Interfaces 6 (2014) 3058-3074 doi: 10.1021/am4058138

[4] A. S. Rogachev, S. G. Vadchenko, F. Baras, O. Politano, S. Rouvimov, N. V. Sachkova, and A. S. Mukasyan, Structure evolution and reaction mechanism in the Ni/Al reactive multilayer nanofoils, Acta Mater 66 (2014) 86-96 doi: 10.1016/j.actamat.2013.11.045

[5] A. S. Rogachev, S. G. Vadchenko, F. Baras, O. Politano, S. Rouvimov, N. V. Sachkova, M.D. Grapes, T.P. Weiss and A. S. Mukasyan, Combustion in reactive multilayer Ni/Al nanofoils: Experiments and molecular dynamic simulation, Combust. Flame (2016) doi: 10.1016/j.combustflame.2016.01.014

[6] T. Duguet, Yong Han, Chad Yuan, Dameng Jing, Baris Unal, J.W. Evans and P.A. Thiel, Self-assembly of metal nanostructure on binary alloy surfaces, PNAS 108 (2011) 989-994 doi: 10.1073/pnas.1008157107

[7] J.H. van der Merle and E. Bauer, Influence of misfit and bonding on the mode of growth in epitaxy, Phys. Rev. B 39 (1989) 3632-3641 doi: 10.1103/PhysRevB.39.3632

[8] V. Shutthanandan, Adli A. Saleh and R.J. Smith, Alloy formation at the Ni-Al interface for nickel films deposited on Al(110) interfaces, Surf. Sci. 450 (2000) 204-226 doi: 10.1016/S0039-6028(00)00050-9

[9] S.-G. Lee and Y.-C. Chung, Surface characteristics of epitaxially grown Ni layers on Al surfaces: Molecular dynamics simulations, J. Appl. Phys. 100 (2006) 074905 doi:10.1063/1.2355440

[10] S. Le Pévédic, D. Schmaus and C. Cohen, Growth of Ni-Al alloys on Ni(111): (I) Formation of epitaxial Ni3Al from ultra-thin Al deposits. Surf. Sc. 600 (2006) 565-576. doi:10.1016/j.susc.2005.11.010

[11] S. Le Pévédic, D. Schmaus, C. Cohen, Growth of Ni-Al alloys on Ni(111) from Al deposits of various thicknesses: (II) Formation of NiAl over a Ni_3Al interfacial layer, Surf. Sci. 601 (2007) 395-410. doi:10.1016/j.susc.2006.10.005.

[12] C.W. Sinclair and R.G. Hoagland, A molecular dynamics study of the fcc $\rightarrow$ bcc transformation at fault intersections, Acta Mat. 56 (2008) 4160-4171. doi: 10.1016/j.actamat.2008.04.043

[13] S. Plimpton, Fast parallel algorithms for short-range molecular dynamics, J. Comp. Phys., 117 (1995) 1-19; http://lammps.sandia.gov/

[14] V. Turlo, F. Baras and O. Politano, Comparative study of embedded-atom methods applied to the reactivity in the Ni-Al system, Modelling Simul. Mater. Sci. Eng. 25 (2017) 064002 doi: 10.1088/1361-651X/aa6cfa

[15] Y. Mishin, M. J. Mehl, D.A. Papaconstantopoulos, Embedded-atom potential for B2-NiAl, Phys. Rev. B 65 (2002) 224114 doi: 10.1103/PhysRevB.65.224114

[16] F. Baras and O. Politano, Molecular dynamics simulations of nanometric metallic multilayers: Reactivity of the Ni-Al system, Phys. Rev. B 84 (2011) 024113 doi: 10.1103/PhysRevB.84.024113

[17] G.J. Ackland and A.P. Jones, Applications of local crystal structure measures in experiment and simulation, Phys. Rev. B 73 (2006) 054104 doi: 10.1103/PhysRevB.73.054104

[18] V.M. Kutznetsov, R.I. Kadyrov and G.E. Rudenskii, Calculation of surface energy of metals and alloys by the electron density functional method, J. Mater. Sci. Technol. 14 (1998) 320-322.

[19] M. Parrinello and A. Rahman, Crystal-structure and pair potentials - a molecular-dynamics study, Phys. Rev. Lett. 45 (1980) 1196-1199 doi: 10.1103/PhysRevLett.45.1196

[20] H.K.D.H. Bhadeshia, Worked examples in the Geometry of Crystals, Second edition, The Institute of Metals©, London (2006)

[21] W. Pitsch, The martensite transformation in thin foils of iron-nitrogen alloys, Phil. Mag 4 (1959) 577-584 doi:10.1080/14786435908238253

[22] D.B. Williams and C.B. Carter, *Transmission Electron Microscopy*, Springer (2009)

[23] M.M. Julian, *Foundations of crystallography with computer applications*, CRC Press (2015)

[24] S.P. Coleman, M.M. Sichani, D.E. Spearot, A computational algorithm to produce virtual X-ray and electron diffraction patterns from atomistic simulations, JOM 66 (2014) 408-416 doi: 10.1007/s11837-013-0829-3

[25] G. Kurdjumov and G. Sachs, Uber den Mechanismus der Stahlhartung, Z. Phys. 64 (1930) 325-343

[26] V. Turlo, O. Politano and F. Baras, Alloying propagation in nanometric Ni/Al multilayers: A molecular dynamics study, J. Appl. Phys. 121 (2017) 055304 doi:10.1063/1.4975474

[27] S.M. Paik and S. Das Sarma, Atomistic growth mechanisms for the molecular-beam epitaxy of a model system, Phys. Rev. B 39 (1989) 9793 doi: 10.1103/PhysRevB.39.9793